vehicles

MDPI

Article

A Development of a New Image Analysis Technique for Detecting the Flame Front Evolution in Spark Ignition Engine under Lean Condition

Luca Petrucci [1,*], Federico Ricci [1], Francesco Mariani [1] and Gabriele Discepoli [2]

[1] Engineering Department, University of Perugia, Via Goffredo Duranti, 93, 06125 Perugia, Italy; federico.ricci4@studenti.unipg.it (F.R.); francesco.mariani@unipg.it (F.M.)
[2] DISMI-Department of Sciences and Methods for Engineering, University of Modena and Reggio Emilia, Via Giovanni Amendola, 2, 42122 Reggio Emilia, Italy; gabriele.discepoli@unimore.it
* Correspondence: luca.petrucci1@studenti.unipg.it

Abstract: The aim of herein work is to develop an automatized algorithm for detecting, as objectively as possible, the flame front evolution of lean/ultra-lean mixtures ignited by low temperature plasma-based ignition systems. The low luminosity characterizing the latter conditions makes both kernel formation and combustion development difficult to detect accurately. Therefore, to estimate the igniter capability to efficiently ignite the mixture, ever more performing tools are required. The present work proposes a new image analysis technique, based on a dual-exposure fusion algorithm and on Convolutional Neural Networks (CNNs), to process low brightness images captured via high-speed camera on an optical engine. The performance of the proposed algorithm (PA) is compared to the one of a base reference (BR) algorithm used by the same research group for the imaging analysis. The comparison shows the capability of PA to quantify the flame radius of consecutive combustion cycles with lower dispersion if compared to BR and to correctly detect some events considered as misfires or anomalies by BR. Moreover, the proposed method shows greater capability to detect, in advance, the kernel formation with respect to BR, thus allowing a more detailed analysis of the performance of the igniters. A metric quantitative analysis is carried out, as well, to confirm the above-mentioned results. Therefore, PA results to be more suitable for analyzing ultra-lean combustions, heavily investigated to meet the increasingly stringent legislation on the internal combustion engines. Finally, the proposed algorithm allows us to automatically estimate the flame front evolution, regardless of the user's interpretation of the phenomenon.

Keywords: convolutional neural network; combustion evolution; low luminosity; image analysis; machine learning techniques

Citation: Petrucci, L.; Ricci, F.; Mariani, F.; Discepoli, G. A Development of a New Image Analysis Technique for Detecting the Flame Front Evolution in Spark Ignition Engine under Lean Condition. *Vehicles* **2022**, *4*, 145–166. https://doi.org/10.3390/vehicles4010010

Academic Editor: Shiyang Tang

Received: 29 December 2021
Accepted: 8 February 2022
Published: 16 February 2022

1. Introduction

Over the last few decades, the development and application of both experimental and computational research have enabled in-depth analysis of fundamental physical phenomena occurring in spark-ignition (SI) internal combustion engines (ICEs) [1,2].

In the ICE experimental research field, the single-cylinder optical access engine is a well-known and widely used diagnostic technique for investigating the temporal evolution of the flame front [3,4]. In recent years, plasma-assisted ignition (PAIs) systems, such as corona effect discharge, nanosecond pulse discharge, microwave-assisted discharge, etc. have been widely studied in optical engines. These systems represent an alternative solution to the traditional spark for facing with future high-efficiency SI engines [5–11].

Focusing on the corona discharge, Idicheria and Najt [12] performed a morphological analysis of the flame front using a gasoline-fueled engine. Marko et al. [13] evaluated the projected flame area on a natural gas fueled engine. They found improvements in *EGR* tolerance using corona instead of conventional spark. The research group of the Department

of Engineering (University of Perugia) found an important extension of the lean stable limit, compared to the traditional spark, at different engine operating conditions [14,15] and using different fuels. The lean extension achieved by such devices [14,15] may be an effective technology to address the objectives of reducing pollutant emissions and fuel consumption. Detection of the first moment of kernel formation can be crucial to characterize the capability of an igniter to initiate robust combustions, especially under lean/ultra-lean mixture conditions [16]. The low luminosity, characterizing these extreme conditions, makes it difficult to recognize the combustion evolution (Figure 1) and, especially, the early flame development. For that reason, the requirements for a more powerful tool capable of recognizing the flame front, led our research group to explore new ways to accomplish this target.

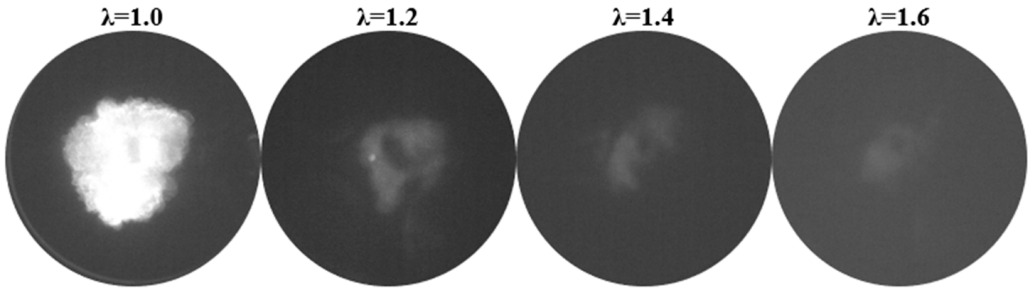

Figure 1. Decrease in brightness as the air/fuel ratio increases.

Currently, artificial intelligence (AI) is increasingly used in the automotive field, as a powerful technique for engine parameter control [17,18], on-board diagnostics (OBDs) [19] and pollutant emissions prediction [20–22]. In the latter area of research, Warey et al. [22] proposed a machine learning (ML) approach using deep CNNs to predict the engine-out emissions. The analysis starts from images generated by CFD simulations, concerning equivalent ratio, temperature, velocity field and turbulent kinetic energy at the exhaust valve opening. CNNs are currently also considered as one of the most powerful tools in the field of image classification [23–25], object and edge detection [26,27] and background noise removal [28,29].

Based on these considerations, the present work proposes a new image analysis technique based on dual-exposure fusion and CNN algorithms, with the aim to improve the flame detection capability of the method used in [14]. In [5], the quantification of the combustion evolution promoted by two different kinds of corona devices was carried out in MATLAB environment. The code performed the operation of filtering, ignition detection and binarization. In the latter process, the filtered grayscale frames are converted to black and white ones to evaluate the burned area (white pixels) and the unburned one (black pixels). The binarization threshold is not fixed, but it is evaluated with a semi-automatic algorithm, proposed by Shawal et al. [30], which guarantees great accuracy in flame evolution detection. The determination of this threshold is mainly performed by the user, which iteratively tries to find the best trade-off between the output of the algorithm and the corresponding original image. Nevertheless, while for stoichiometric conditions the user task is simplified by high luminosity, the low brightness characterizing lean operations complicate the identification of the early flame development [16].

Starting from the results of [14], CNNs methodology is first optimized on the flame front images of a weakly lean case to determine the most suitable structure according to the aim of the work. After the validation, the proposed algorithm (PA) is tested on the lean stable limits performed by the ACIS devices. To evaluate the performance of the algorithms, the corresponding results are compared by estimating the equivalent flame radius R_{eq} of each combustion event [14].

The PA method is able to reproduce the BR results, in particular, correctly detecting each combustion, unlike the BR method, which mistakenly considered some events as anomalies. Moreover, each event is detected in advance, namely, up to 9 crank angle degrees (corresponding to 1500 μs) before the BR detection. This fundamental feature allows us to identify the flame formation as early and accurately as possible at the moment of its first effective creation. Finally, the recognition of the flame evolution is carried out by PA, regardless of the any user's decision, which could make the proposed method potentially suitable for any type of application requiring a high degree of objectivity.

2. Experimental Setup

2.1. Optical Access Engine

Tests were carried out on a 500-cc single-cylinder research engine optically accessible (Figure 2a), with pent-roof combustion chamber, four valves, and a reverse tumble intake port system which is designed to operate in direct injection (DI) or port fuel injection (PFI). The latter configuration was used, with the igniter centrally located (Figure 2b). The internal cylinder bore is 85 mm while the piston stroke is 88 mm. The compression ratio is about 2 points lower than actual commercial automotive SI engines, but belongs to a well-studied range, featured with an optimal compromise between power output and thermal efficiency [31].

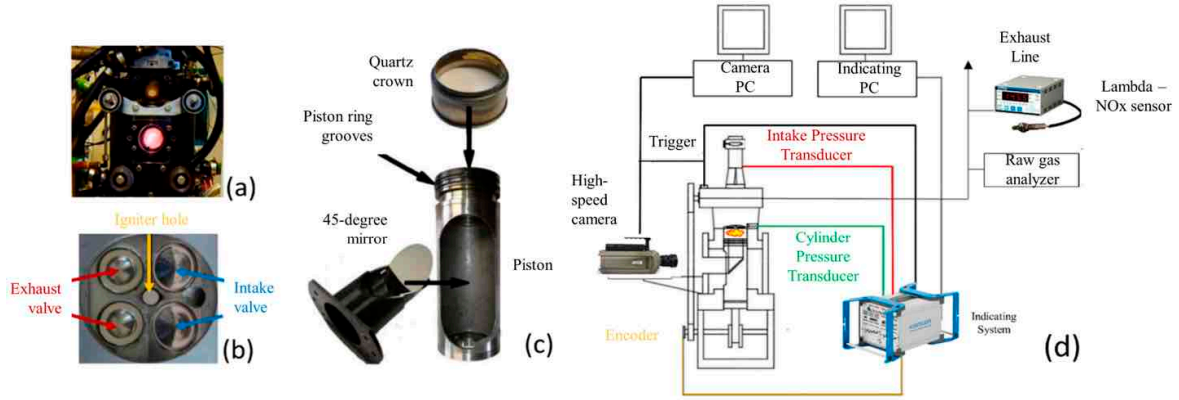

Figure 2. Details of the (**a**) optical access engine, (**b**) engine head, (**c**) optical apparatus and (**d**) schematization of the measurement apparatus.

The optical access to the engine combustion chamber is guaranteed by a 45-degree mirror and a Bowditch piston with a 60 mm quartz crown (Figure 2c). Both quartz and mirror are designed to allow light transmission in the visible range. Piston rings are realized in a self-lubricant material, i.e., a Teflon–graphite mix, since a dry contact between cylinder liner and rings is required.

For all the other moving parts of the engine, a conventional mineral lubricant was used as follows: its temperature, together with the coolant one, was set at 343.0 ± 0.2 K. This value was chosen to guarantee longer engine durability and a reduced blow-by [32].

An AVL 5700 dynamic brake, coupled with the crankshaft, ensures the engine speed control both in motored and firing condition. Standard European market gasoline (E5, with RON = 95 and MON = 85) is injected by a Weber IWP092 port fuel injector at 5 bar absolute. The air-fuel ratio (λ) is modified by varying the fuel amount at fixed throttle position, in order to maintain the same turbulence level inside the combustion chamber. An Athena GET HPUH4 engine control unit (ECU) controls the injector energizing time and the ignition timing, by sending a trigger signal to the dedicated control units of the igniters. The intake port pressure is recorded by a piezoresistive transducer (Kistler 4075A5) and a piezoelectric transducer (Kistler 6061 B), placed on the side of the chamber, measures the in-cylinder pressure. The indicated analysis (Figure 2d) is performed through a Kistler Kibox combustion analysis system (temporal resolution of 0.1 CAD) that acquires the pressure

signals, the λ measured by a fast lambda probe at the exhaust pipe (Horiba MEXA-720, accuracy of ±2.5%), the ignition signal from ECU, the absolute crank angular position measured by an optical encoder (AVL 365C), and the trigger signal used for synchronization purposes. Moreover, the exhaust gas analysis was performed by a Horiba MEXA 7100D with an OVN 723-A.

For each operating point tested, a total of 100 consecutive combustion events were recorded. The determination of the total injected fuel mass was performed after engine tests through a Micron AD scale (±10 mg accuracy) after 20,000 consecutive injection events at the same gasoline pressure and injector *ET*; the mass per cycle (i.e., the dynamic flow rate Q according to SAE J1832 [33]) was then computed.

2.2. Imaging System

The natural luminosity [34,35] of streamers and flames is recorded by a Vision Research Phantom V710 high-speed CMOS camera coupled with a Nikon 55 mm f/2.8 [36]. A common trigger signal, derived from an automotive camshaft position sensor (Bosch 0232103052), ensures the synchronization between imaging data and indicating ones, thus allowing to match flame development 2D information (on a swirl plane) and in-cylinder pressure trace of the same cycle (Figure 3).

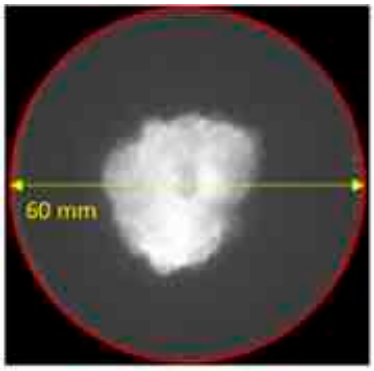

Figure 3. Area of the combustion chamber framed by the high-speed camera through the optical access (diameter equals to 60 mm).

The high-speed camera starts recording when the rising edge of the trigger signal is detected. A tunable pre-trigger length allows us to set several frames to be acquired even before the rising edge. Due to flame wrinkling, distortion and convection, the flame average radius detectable without reaching the optical boundary is 20 mm, corresponding to about 5% of mass fraction burned (MFB) [37].

According to the characteristics of the optical apparatus [36], in [5] each frame was composed of 512 × 512 pixel to detect the whole flame evolution inside the optical limit. The maximum allowable sampling rate of 20 kHz was used, corresponding to a temporal resolution of 0.3 CAD/frame at 1000 rpm. For each point tested, 63 consecutive combustions were recorded. A summary of the main optical parameter is shown in Table 1.

Table 1. High-speed camera settings.

Feature	Value	Unit
Image resolution	512 × 512	pixel
Sampling rate	20	kHz
Exposure time	49	µs
Bit depth	8	bit
Spatial resolution	124	µm/pixel
Temporal resolution (@1000 rpm)	0.3	CAD/frame

An in-house MATLAB code allowed us to extract quantitative information from the gray-scale combustion images acquired by the high-speed camera. In the following sections, a detailed description of the algorithms used in [5] can be found.

2.3. Igniters

The experimental campaign was developed by using two different radio-frequency (RF) advanced corona igniters, the Barrier Discharge Igniter (BDI) and Corona Streamer-type Igniter (CSI), provided by Federal Mogul Powertrain—a Tenneco group company. *BDI* [38] is made up of a grounded annular extension from which ionization waves, named streamers, start to propagate towards the top of the alumina globe that overlaps the high-electrode voltage [38,39] (Figure 4). In the CSI [40,41] configuration (Figure 4), the streamers start from four-tip electrode and propagate into the medium towards the counter-electrode (piston head and chamber walls of the optical engine). Considering the optical configuration of [5], in the spark case (Figure 4), the visualization of the flame kernel formation is hampered both by the low mixture volume involved during the discharge and by the igniter geometry. At lean condition, i.e., low luminosity, the optical acquisition becomes even more complicated. Conversely, ACISs can spatially involve a considerable amount of mixture through volumetric discharges (Figure 4).

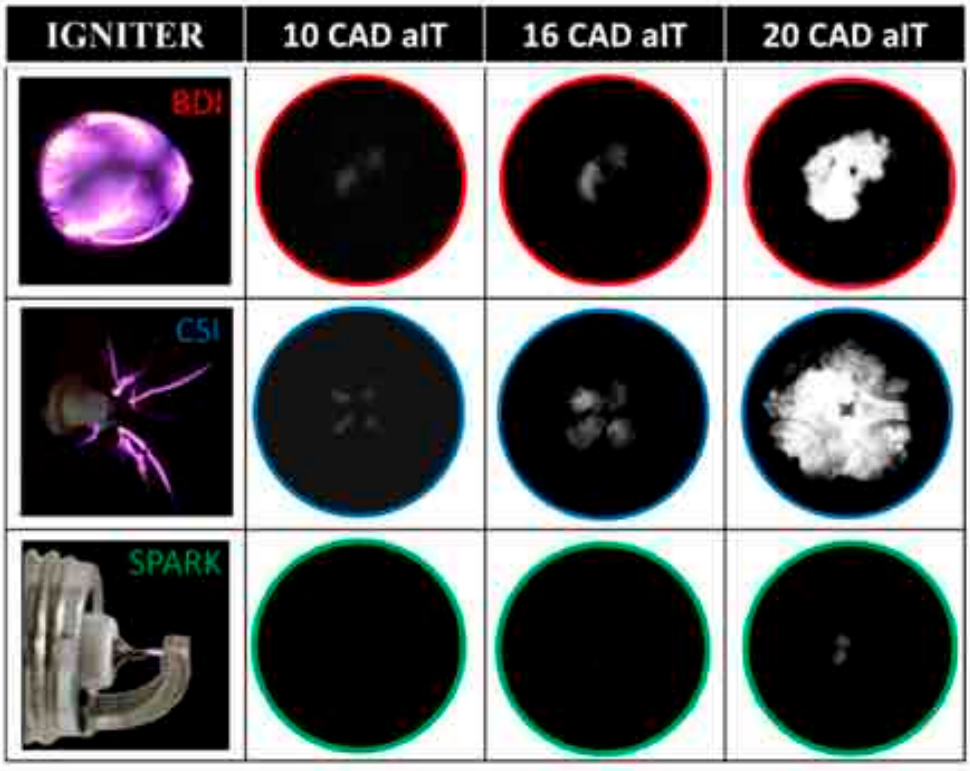

Figure 4. Representation of the flame front evolution in the first instant after the end of the discharge (aIT = after ignition timing), both for ACIS devices (BDI and CSI) and traditional spark, at air-fuel ratio equal to 1.4. It is possible to observe at 10 CAD aIT as the volumetric discharges characterizing the corona devices allow a better detection of the combustion evolution if compared to the spark-case.

Upon receiving the trigger signal from the ECU, corona igniters are powered by a dedicated electronic system (ACIS Box) with an input radio-frequency of about 1.04 MHz, corresponding to the resonance frequency of the equivalent RLC circuit [24]. Both corona igniters can be modeled by a same lumped-parameter circuit [34,41]. Corona behavior is controlled by managing two setting parameters, namely, driving voltage (V_d) the corona duration (t_{on}). The first one, proportional to the electrode voltage [41], is responsible for the corona development, whose penetration into the medium depends on the working

conditions. The corona duration represents the activation time of the igniters and plays an important role in reducing the cycle-to-cycle variability [40]. Once V_d is set, the electronic system magnifies the voltage up to a proportional value (supplied voltage, V_s) and provides it to the coil. This latter amplifies the voltage to the firing-end up to V_e in order to produce the discharge.

3. Methods

In this section, the authors discuss the structures and the functionalities of both the algorithm used in [14] and the one proposed in this research activity.

3.1. Base Reference Algorithm

The BR algorithm, dedicated to the post-processing of the combustion images (Figure 5a), performs the operations of ignition detection, image filtering (Figure 5b), and binarization of the frames (Figure 5c) [36].

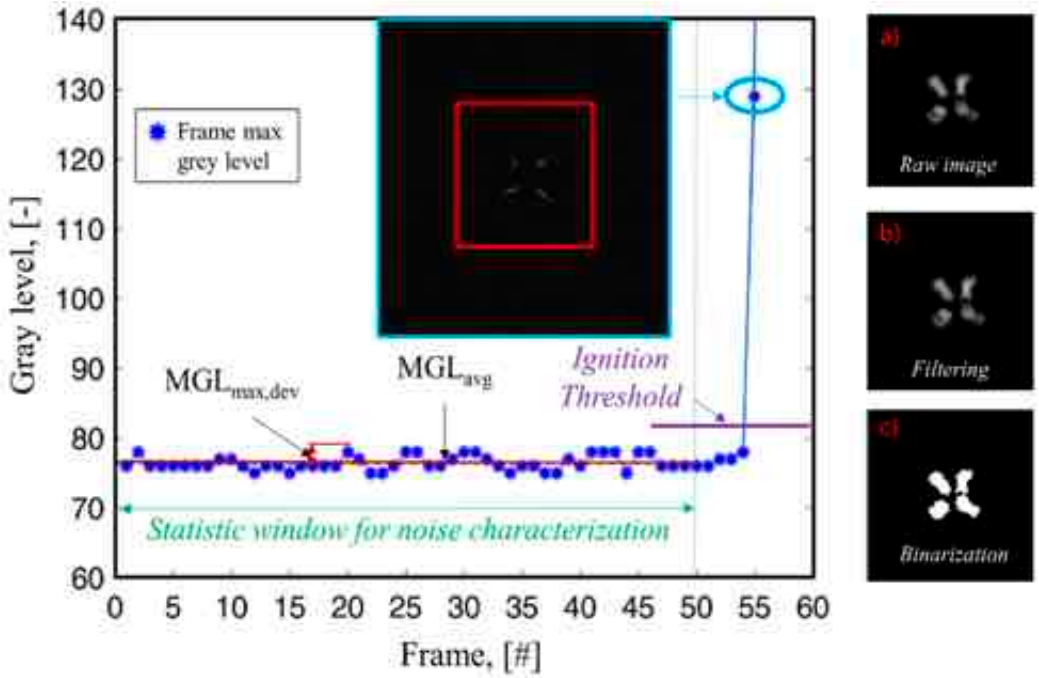

Figure 5. Example of maximum grey level evolution in the statistic window preceding the ignition event (first ignition frame): the red square is the sub-area for ignition detection. The images on the right side display the main steps of the combustion analysis performed on the (**a**) original image, i.e., (**b**) filtering and (**c**) binarization processes.

1. Filtering—the filtering process is carried out on each recorded image by means of a 3 × 3 pixel median spatial filter, in order to reduce the salt and pepper noise. The filter is featured with variable dimension depending on images luminosity and contrast.
2. Ignition Detection—Power-on detection is based on a frame-by-frame maximum gray level (MGL) detection on a centrally located sub-area of 220 × 220 pixel. The MGL of each frame is equal to the highest value recorded in such area. A statistically significant number of frames before switching on, i.e., 50, is chosen first and the average of the maximum gray level MGL_{avg} (Equation (1)) in such windows is calculated, together with the maximum absolute deviation from the mean $MGL_{max,dev}$ (Equation (2)) (Figure 5).

$$MGL_{avg} = \frac{1}{n}\sum_{j=1}^{n} MGL_j \quad (1)$$

$$MGL_{avg,dev} = \max_{1 \le j \le n} \{MGL_j - MGL_{avg}\} \quad (2)$$

with:

n = dimension of the statistic window

j = frame index in the statistic window ($j \le n$)

The detection condition of the first ignition event (Figure 5) is therefore expressed as follows (Equation (3)):

$$MGL_i > MGL_{avg} + K \times MGL_{max,dev} \quad (3)$$

where:

i = frame index after the statistics window ($i > n$)

K = arbitrary constant

3. Binarization—finally, a binarization of the image is carried out to convert from grayscale frames to black (unburned area) and white (burned area) ones with the aim to determine the equivalent flame radius R_{eq} (Equation (4)), starting from the knowledge of equivalent flame area A_{eq}. For each frame, A_{eq} in mm^2 is obtained by computing the sum of the pixels representing the flame front (value equal to 1).

$$A_{eq} > \pi \times R_{eq}^2 = n_b \times sc^2 \quad (4)$$

where:

R_{eq} = equivalent flame radius

n_b = number of binarized pixels

sc = scaling factor [mm/pixel]

The binarization threshold is not fixed but is evaluated for each frame with a dynamic semi-automatic algorithm [30]. Starting after the first ignition event detected, the threshold TH of each subsequent image is set proportionally to the average grey level AVG_j of the previous image, as shown in the following (Equation (5)):

$$TH = AVG_j \times K_1 + K_2 \quad (5)$$

After choosing the best pair (K_1,K_2), the method is applied to all 63 combustions analyzed. Given that the threshold values strongly depend on the average luminosity level of each event, some combustions could therefore be considered as anomalies instead of regular events, thus making the (K_1,K_2) unfit for the analysis. This aspect will be covered in detail in the Section 5. Whereas for stoichiometric mixtures, the BR analysis is made easier by the strong brightness of the event, for high λ values, the user could encounter significant difficulties, in particular to distinguish the beginning of the combustion event. Since, nowadays, the automotive research field is aimed at the investigation of technologies able to operate with increasingly lean mixtures, the post-processing of growing less luminous images may be an essential activity to focus on. The recognition of the flame front in ultra-lean condition becomes an increasingly delicate operation that requires progressively more advanced and sophisticated algorithms. The arbitrariness of choice is fine as long as the flame front is well-defined. At extreme operating condition, this arbitrariness becomes excessive, and different operators could produce quite different results and, therefore, of questionable value. Indeed, in the BR method, the determination of the whole flame evolution depends on parameters suggested by the user's phenomenological interpretation of the phenomenon. During the analysis of less bright images, the operator struggles to identify the flame front in the first moments of combustion.

For all these reasons, in this work, an alternative method capable of detecting the flame front in an objective manner has been sought to overcome the abovementioned problems.

3.2. Proposed Algorithm

Generally speaking, the opacity of the images due to the presence of quartz on the piston head, the reverberation of reflecting bodies placed inside the combustion chamber and the lack of brightness due to lean mixtures, represent the main issues which make difficult the physical interpretation of the flame front evolution. Moreover, the progressively increase in residuals on the optical access highly affects the quality of the recorded images by enhancing, cycle-by-cycle, the haze effect.

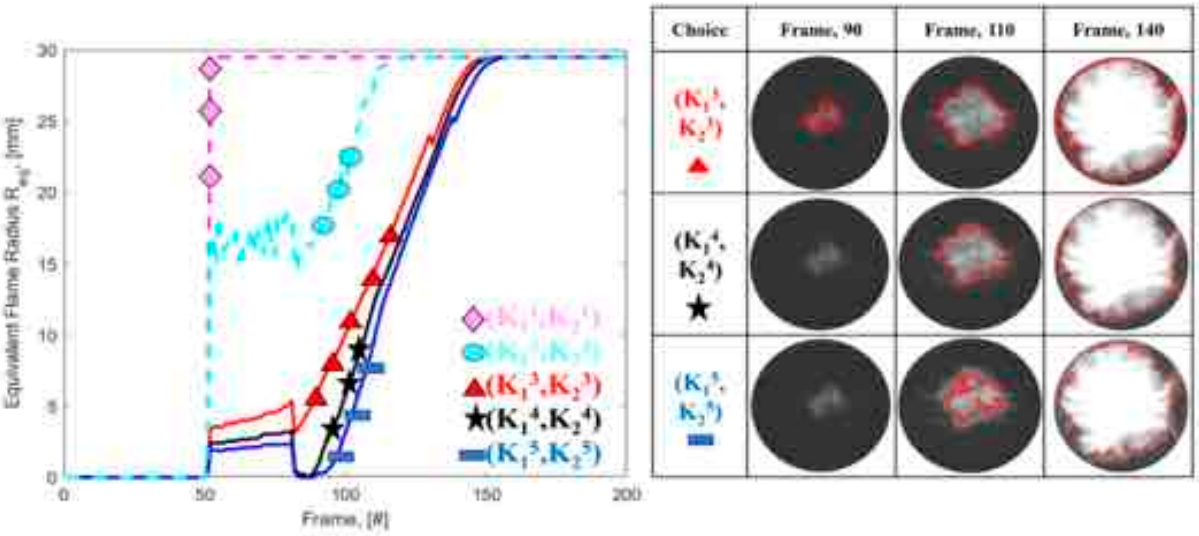

(**a**) (**b**)

Figure 6. (**a**) Examples of R_{eq} not suitable to reproduce the increasing trend of the flame radius during the development of the combustion process and R_{eq} (solid lines) that may be considered potentially suitable for reproducing the same combustion physical phenomenon. (**b**) The figures on the right depict the contouring process, for the potentially right cases, applied to detect the capability of BR in reproducing the flame front of the original images. (K_1^3, K_2^3) choice allows to better reproduce the flame front and therefore can be considered as the best choice to select.

Based on these considerations, the detection could be simplified by using specific filters for brightness/contrast enhancement, and haze removal to limit the alteration of the information of the images.

Concerning the brightness and contrast enhancement, Ying et al. [42] proposed an algorithm, named BIMEF, that involves the use of an image fusion technique similar to high dynamic range, and comparable to the post-processing happening in our brain. Inspired by the human visual system, they design a multi-exposure fusion framework for low-light image enhancement, by proposing a dual-exposure fusion algorithm to provide an accurate contrast and lightness enhancement. In output, the algorithm returns an image with less distortion of brightness and greater fidelity to visual information than the other known algorithms in the literature (for example LIME and NPE) [43,44].

Based on these considerations, the algorithm of Ying et al. [42] is employed in the present work for enhancing the luminosity of our low-brightness images.

Concerning the haze removal, Li, B. et al. [45] propose an efficient end-to-end dehazing convolutional neural network model, called the All-in-One Dehazing Network (AOD-Net). They compare the proposed model with a variety of state-of-the-art methods, on both synthetic and natural haze images, using both objective and subjective measurements. Once the intensity of the haze is estimated, five convolutional layers clear the haze from the image. Extensive experimental results confirm the excellent, robustness, and efficiency of AOD-Net [45].

Based on these considerations, the algorithm of Li, B. et al. [45] is chosen in the present work for limiting the effects of reverberation and opacity which affect the recorded images.

The present work evaluates the quality of the images processed by the abovementioned algorithms through the following two different parameters: the structural similarity index map (SSIM) and the peak signal-to-noise ratio (PSNR) [46,47].

PSNR is commonly used to quantify the quality of reconstruction for lossy compression images and videos. It is defined as the ratio between the maximum signal power MAX and the noise signal power. This parameter is calculated by the mean squared error MSE as follows [47]:

$$\mathrm{PSNR} = 20\log_{10}(\mathrm{MAX}/(\mathrm{MSE})^{1/2}) \quad (6)$$

SSIM is a method for predicting the perceived quality of digital images or video. It is also used for measuring the similarity between two images [47].

$$\mathrm{SSIM}(x,y) = \frac{\left(2\mu_x\mu_y + C_1\right)\left(2\sigma_{xy} + C_2\right)}{\left(\mu_x{}^2 + \mu_y{}^2 + C_1\right)\left(\sigma_x{}^2 + \sigma_y{}^2 + C_2\right)} \quad (7)$$

where x and y are the windows dimensions of the image, μ and σ are the average and variance value of the specific dimension of the frame, respectively, σ_{xy} the covariance and C_1 and C_2 two variables to stabilize the division with weak denominator.

Based on the previous considerations, preliminary tests were carried out at $\lambda = 1.4$ to determine, from the original images, the method structure, namely, the most suitable steps-sequence (Table 2) according to the purpose of the work.

Table 2. List of the analyzed cases to determine the best algorithm sequence for the proposed method.

Cases	Sequences
A	BIMEF
B	DEHAZING
C	BIMEF+DEHAZING
D	DEHAZING + BIMEF
E	BIMEF+DEHAZING+DENOISING

For each evaluated combination (single step or multiple steps), Table 3 shows the PSNR and SSIM values used to determine the method structure. At each specific CAD aED (after end of discharge), reported in Table 3, PSNRs and SSIMs are computed as the average value of 63 PSNRs and SSIMs (equal to the number of consecutive recorded combustion events). For sake of completeness, Table 3 displays, through images of the combustion flame, the outputs of the algorithms reported in Table 2. The combination showing the highest values PSNR and SSIM has been chosen. Single step procedures [(BIMEF(A) and DEHAZING (B)] result in being unfit to guarantee filtered images simultaneously characterized by high values of fidelity (high SSIM and high PSNR).

The two-step procedure (C combination) has been chosen since it presents both the highest value of SSIM and PSNR if compared to the ones obtained using D. Once the most suitable sequence is established, a denoising action is implemented to reduce the salt and pepper noise which affect the dehazing process. This undesired effect could alter the result in the subsequent binarization phase, detecting illuminated pixels belonging to the background as a flame front. The FFDNet algorithm, proposed by Kai Zhang et al. [48], is used in this work. Starting from the estimation of the mean noise level of the 20 frames before the start of discharge, the algorithm subtracts it from each frame of the recorded series. The algorithm is a three-layered CNN, mainly composed of the following three operations: convolution, batch normalization and Relu. It uses the orthogonal initialization method with convolution filters that allow the noise level map to effectively control the trade-off between noise reduction and detail retention. Denoising occurs via a non-uniform

map that removes noise spatially variable. This latter step allowed to increase both SSIM and PSNR of the combination C, as reported in the final combination E (Table 3).

Table 3. Outputs of the algorithms reported in Table 2, at each specific CAD aED. PSNRs and SSIMs are computed as the average value of 63 values (equal to the number of consecutive recorded combustion events).

CAD aED	Original Frames	A		B		C		D		E	
		SSIM	PSNR	SSIM	PSNR	SSIM	PSNR	SSIM	PSNR	SSIM	PSNR
8	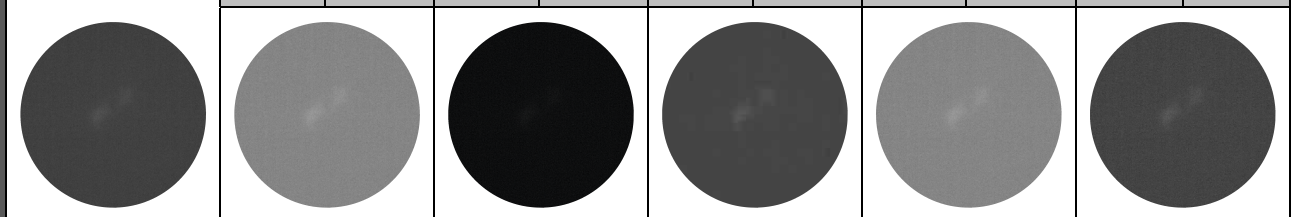	0.76	11.6	0.42	14.1	0.84	31.6	0.40	11.3	0.95	35.5
15	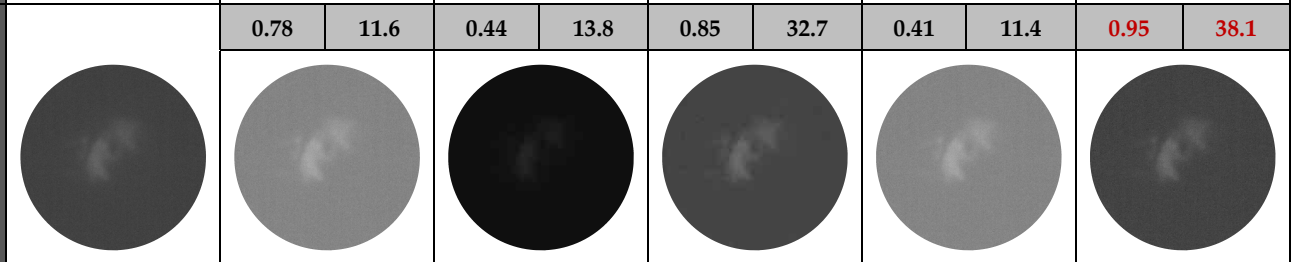	0.78	11.6	0.44	13.8	0.85	32.7	0.41	11.4	0.95	38.1
22	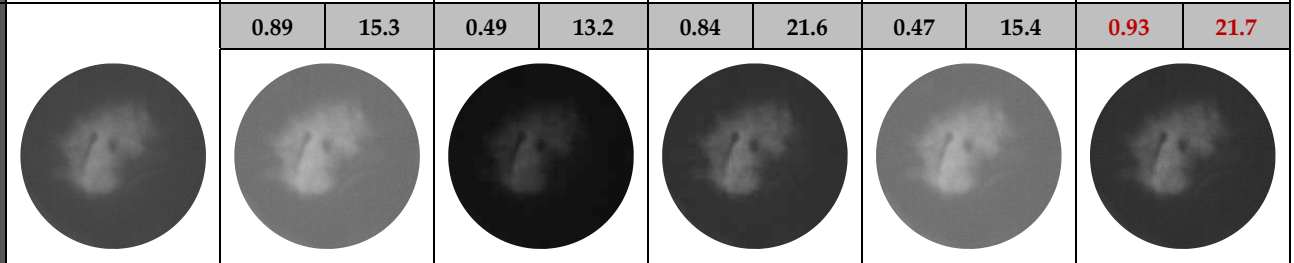	0.89	15.3	0.49	13.2	0.84	21.6	0.47	15.4	0.93	21.7
29	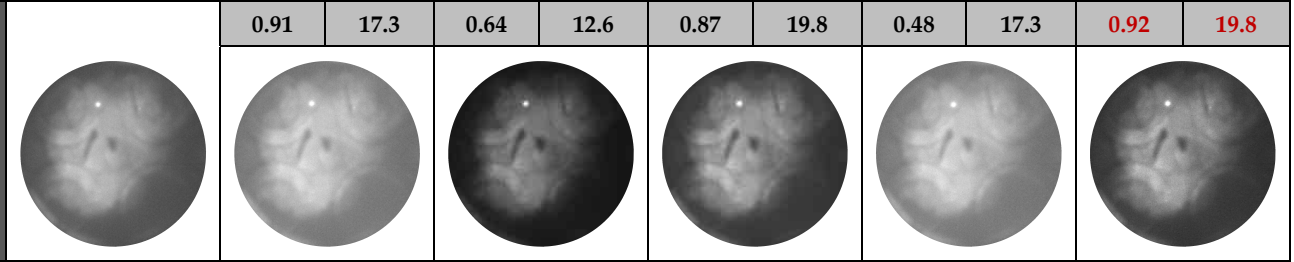	0.91	17.3	0.64	12.6	0.87	19.8	0.48	17.3	0.92	19.8
36	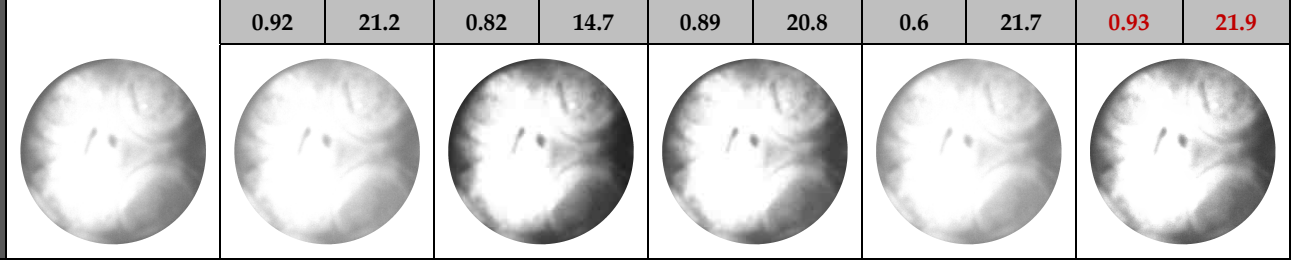	0.92	21.2	0.82	14.7	0.89	20.8	0.6	21.7	0.93	21.9

Starting from the grayscale images (0–255), the last step involves the binarization process to estimate the flame front area. The binarization threshold is automatically set by the algorithm, analyzing the greyscale matrix of Figure 7C which is equal to the first grey scale value with a non-zero number of pixels (Figure 7B) on the first image after the end

of discharge (Figure 7A). The grey scale values of the subsequent images are expected to be higher than the previous one, therefore the same selected threshold value is applied to such frames.

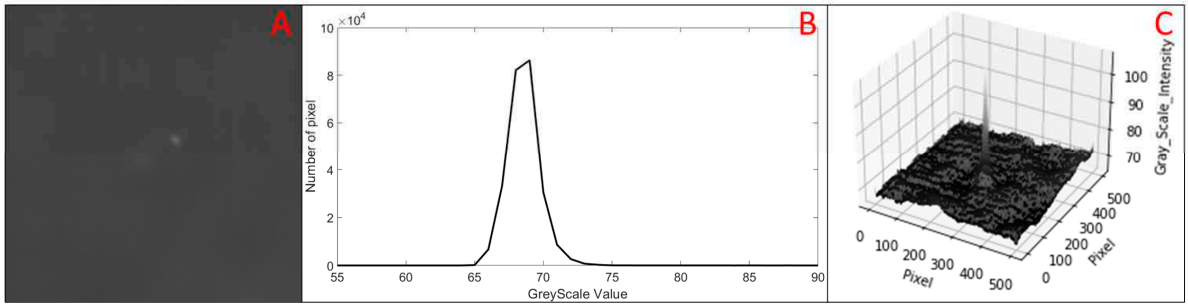

Figure 7. The first image after the end of discharge (**A**) with the corresponding grey scale value distribution of its pixels (**B**) and the grey scale histogram (**C**) utilized by the algorithm to set the binarization threshold.

Since the combustion processes generate dirt residues that produce dirty "black spots" that obscure the analyzed area, the code is also enriched with a contours function. Such function highlights the external flame front by recognizing the morphology of the border, and then fills any holes placed inside it. In such a way, it is possible to give a physical meaning to the phenomenon. In fact, since the combustion process develops from a central point and radially propagates, no holes inside the boundary are physically allowed. The final procedure presented in this work is reported in Figure 8.

Figure 8. Step-by-step results (from **B**–**E**) of the image analysis carried out with PA on the original image (**A**).

For sake of clarity, Figure A1 (Appendix A) displays both the results of the binarization process applied to the images of Table 3 and the one obtained using BR algorithm. Moreover, Figure A2 shows the equivalent flame radius of the analyzed algorithm at $\lambda = 1.4$ to highlight how each structure of Table 2 influences the final interpretation of the physical phenomenon.

4. Test Campaign

The proposed method is fine-tuned working on the image-set acquired in BR. In this wok, the capability of CSI and BDI to extend the lean optical engine stable limit with respect to the traditional spark ($\lambda = 1.4$) is shown [14]. Test were carried out with the engine operating at 1000 rpm and low load (IMEP = 4.5 bar at $\lambda = 1$) [14]. Both igniters were tested by using extreme setting parameters. With a reasonable margin to prevent coil overheating issues, the activation time t_{on} was set equal to 1500 µs. For BDI, the maximum allowable V_d (i.e., equal to 60 V) to prevent igniter malfunction was chosen, whereas CSI was featured with the highest V_d not to face with arching events.

The ignition timing was optimized for each operating point tested with the aim to achieve the maximum brake torque (MBT) (reached with the combustion center MFB50 ≈ 9 CAD aTDC) [37]. CSI and BDI showed similar lean tolerance, with CSI being able to reach a slightly higher value (λ = 1.60, against 1.55 of BDI).

For the sake of clarity, each tested point was considered stable if featured with an CoV_{IMEP} less than 4% [36].

PA methodology is developed starting from an image set of a BDI case, namely, λ = 1.4. Upon being optimized, the algorithm was tested on the lean stable limits performed by the ACIS (λ = 1.60 for CSI and 1.55 for BDI), for a total of three cases analyzed. For the sake of completeness, the main technical characteristics of the abovementioned tested points are reported in Table 4.

Table 4. Main technical characteristics of the experimental points of chosen to develop and test CNNs methodology.

Igniter Type	Engine Speed, (pm)	λ, (-)	V_d, (V)	t_{on}, (μs)	IT, (CAD aTDC)	IMEP, (bar)	COV_{IMEP}, (%)
BDI	1000	1.4	60	1500	−36	3.6	1.5
BDI		1.55	60	1000	−53	3.2	2.3
CSI		1.6	17	1000	−47	3.1	3

5. Results and Discussion

The proposed method is preliminarily validated on a specific combustion event at λ = 1.4, by comparing the PA output with binarized images obtained via human perception and used as Target. The flame front contours are manually identified by the users on the original images and the pixels inside such defined perimeter are white-filled, whereas all the others, not belonging to the flame, are black-filled. The comparison is carried out taking into account characteristic moments of the combustion development, from the kernel formation to the optical limit occlusion (Figure 9). The corresponding binarized areas are compared by evaluating the equivalent flame area A_{eq} (Equation (4)). For the sake of clarity, each image of Figure 9 is cropped around the optical access boundary, corresponding to an area of 2827 mm^2. As visible, PA is able to reproduce the shape and area of the Target images. The differences in terms of A_{eq} quantitatively show the effectiveness of PA. The first image shows a slight overestimation (green flame area) of PA, testified by a difference of 459 pixels, corresponding to 7.28 mm^2 out of a total of 85 mm^2. In other words, PA performs an error of about 9% in estimating the Target area. In the following images, PA slightly underestimates (violet flame area) the Target area; however, the error remains between 4% and 10%.

Since the committed errors can be considered of circumstantial evidence, the PA method is then applied to all the 63 combustions with λ = 1.4. The results are then compared both with Target and the one of BR [14].

Starting from the 63 combustion cycles recorded by the high-speed camera during the test (Table 4), all the equivalent flame radii (R_{eq}) of PA and BR cases are computed. In Figure 10 the R_{eq} evolution is plotted from the instant of the end of the discharge onwards (aED). The colored trend (red for BR and blue for PA) represents the average values of 63 consecutive events. The proposed algorithm reproduces the evolution of the flame front of BR. Moreover, it should be emphasized that PA curves bundles are less wide and, therefore, characterized by lower dispersion. To highlight that, the boxplot of each method displays, through vertical bars, the standard deviation (σ_{Req}) of the equivalent flame radius R_{eq}. For clarity, σ_{Req} values are reported every 10 frames (corresponding to approximately 3 CAD, from the first frame after the end of the discharge. Both methods show a progressively increase in σ_{Req} up to 26.7 CAD. After that, σ_{Req} decreases as it reaches the optical limit. In any case, the PA method performs lower dispersion values.

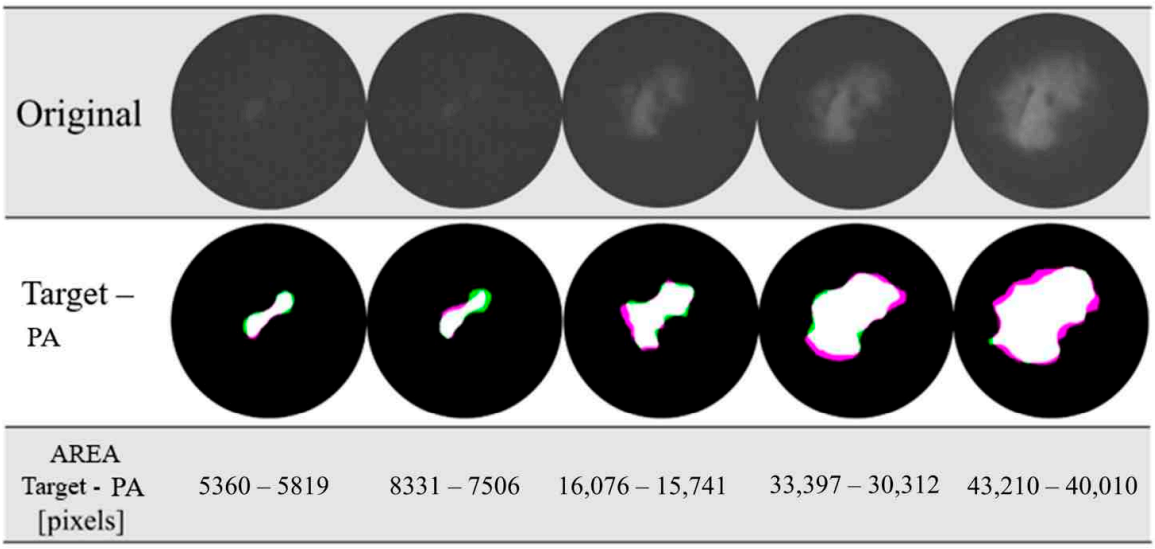

Figure 9. Overlap of the binarized Target images and CNN ones and quantification of the corresponding equivalent flame area. The overestimation is indicated by green flame area whereas the underestimations with violet.

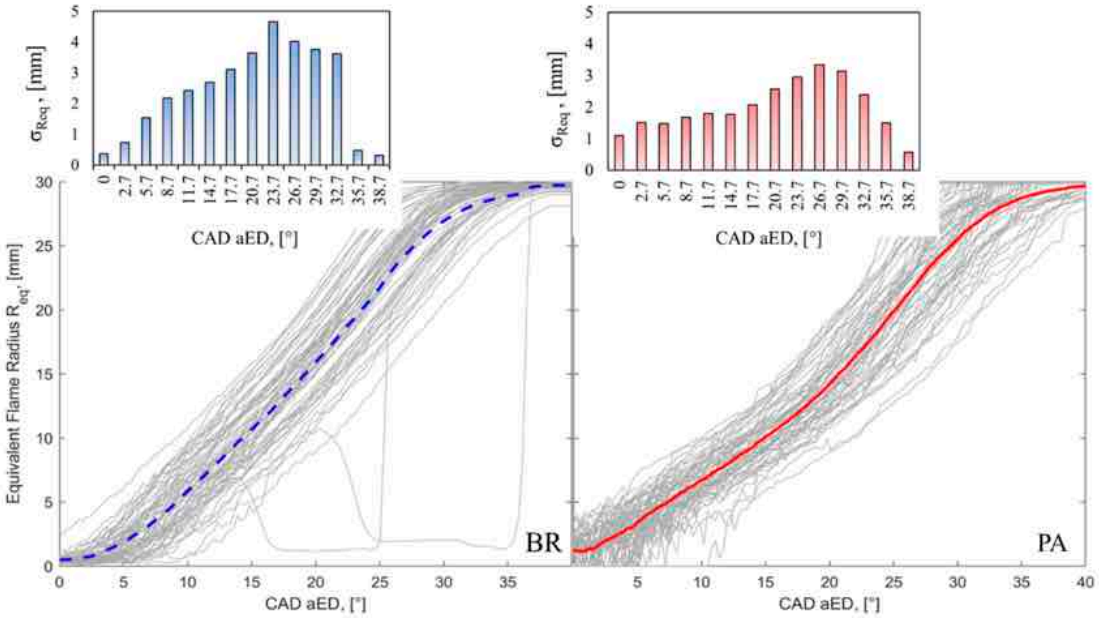

Figure 10. Evaluation of the dispersion on 63 consecutive combustion cycles, in terms of R_{eq}. the corresponding box plots display, through vertical bars, the standard deviation (σ_{Req}) of the equivalent flame radius R_{eq} each 10 frames.

Given that in BR the binarization threshold is substantially determined by the user, the higher dispersion showed (Figure 10) could be due to the difficulty of choose the right threshold capable to correctly estimate the R_{eq} of all events. Therefore, some combustions previously considered by the BR method as misfires or anomalies, are instead considered as physically valid by PA. To demonstrate it, Figure 11 displays the R_{eq} trends and corresponding original frames (after BIMEF operation, for sake of clarity) of the two cases mistakenly recognized as non-physical by BR. For both cases analyzed, both methods identify, even if with a slight delay (see the first images around 8 CAD aED), the first moments of the flame front evolution. In any case, the PA method correctly tracks the combustion evolution, unlike BR, which does not detect the flame front at many CADs.

The corresponding equivalent flame radii (solid lines for PA and dashed one for BR) certify this assertion, showing the progressive evolution of R_{eq} over the CAD.

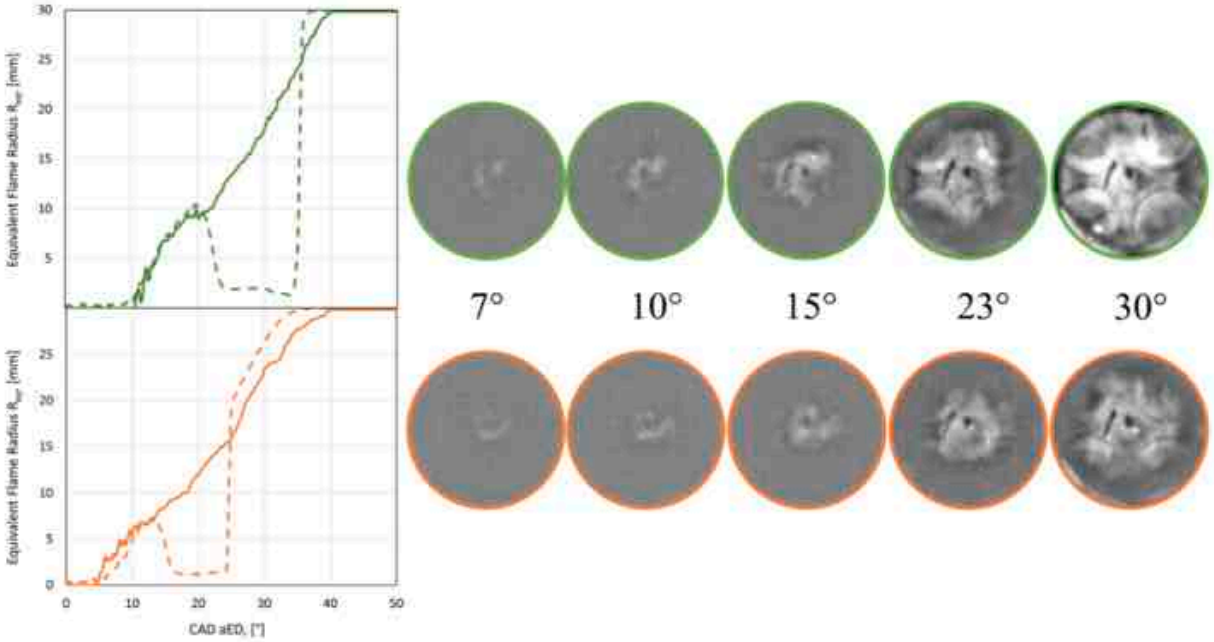

Figure 11. Evaluation of the flame front in order to evaluate the actual existence of the combustion detected as an anomaly by the BR code.

Figure 12a shows the mean R_{eq} trend of the 63 combustions for PA (red curve) and BR (dashed blue line), to be compared with a Target (black markers). Each marker, relating to the specific frame, is determined by averaging 63 R_{eq} values. The procedure is manually performed for each combustion event in order to test the validity of PA. However, it is unthinkable to apply this type of procedure when dealing with large amount of data.

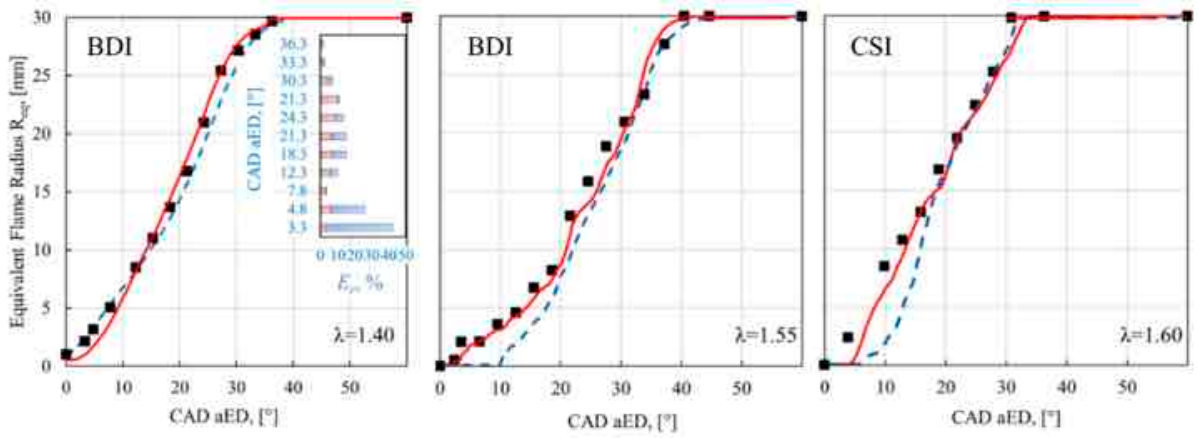

(**a**) (**b**) (**c**)

Figure 12. Evaluation of the R_{eq} trends, averaged over 63 cycles, in the three operating conditions analyzed, i.e., (**a**) λ = 1.4, (**b**) λ = 1.55 and (**c**) λ = 1.6.

As shown in Figure 12a, both methods are able to correctly reproduce the Target trend and, in particular, PA shows a greater capability to detect in advance the kernel formation. To better underline that, the box plot in Figure 12a displays, through vertical bars, the relative percentual errors ($Err = \left|\left(R_{eq}^{Method} - R_{eq}^{Target}\right)/R_{eq}^{Target}\right| * 100$) made by the methods

in estimating the Target values. Higher Err values characterize the BR method in the first CAD, with peaks of up to 40%. From the 7.8 CAD aED, both methods well reproduce the Target. Anyway, the PA percentual error stands below 10%. The obtained results certify the validity of the PA. For that reason, the PA algorithm is applied to the extreme lean operating points of [5]. In order not to dwell on the discussion, Figure 12b,c only report the mean R_{eq}, at $\lambda = 1.55$ (BDI case) and $\lambda = 1.60$ (CSI case). Both methods correctly reproduce the Target trends, and, even in these cases, PA shows greater capability to detect the first moment of the kernel formation. This quality is essential prerogative to characterize the ACIS igniters capability to guarantee an earlier flame development in relation to the spark one.

As mentioned in the Method section, the low luminosity made it difficult to determine the correct binarization threshold for BR algorithm. Therefore, both the corresponding R_{eq} curves are featured by delayed growths. However, from $R_{eq} = 15$ mm, the methods reproduce, with extreme accuracy, the Target curve evolution.

To demonstrate the effectiveness of PA to recognize in advance the front evolution, a complementary analysis is carried out (both Figure 13a,b, refer to $\lambda = 1.6$ case) by overlapping the corresponding images. The areas (red contour for Target, orange area for PA and white area for BR) are superimposed to visualize the flame-front evolution at each CAD. This additional analysis is necessary to highlight how the PA method, despite a slight underestimation of the front with respect to the Target, still obtains a much better result than the BR method, which, for about 15 CAD, practically does not detect the combustion phenomenon (Figure 13).

The performances of the PA method are quantified through the performance evaluation metrics [49] Equations (8)–(10), based on the raster values of the binarized images (Target). The purpose is to evaluate any overestimation and/or underestimation performed by the algorithms. The pixels correctly detected are indicated as true positive (TP), as true negative (TN) those correctly indicated as not belonging to the edge, as false positive (FP) those where the algorithm has mistakenly detected the edge and as false negative (FN) those where the algorithm has mistakenly not detected the edge. Based on those metrics, the accuracy, sensitivity, and specificity of the model were computed as below:

$$\text{Sensitivity} = \frac{(\text{TP})}{(\text{TP} + \text{FN})} \tag{8}$$

$$\text{Specificity} = \frac{\text{TN}}{(\text{TN} + \text{FP})} \tag{9}$$

$$\text{Accuracy} = \frac{(\text{TP} + \text{TN})}{(\text{TP} + \text{TN} + \text{FP} + \text{FN})} \tag{10}$$

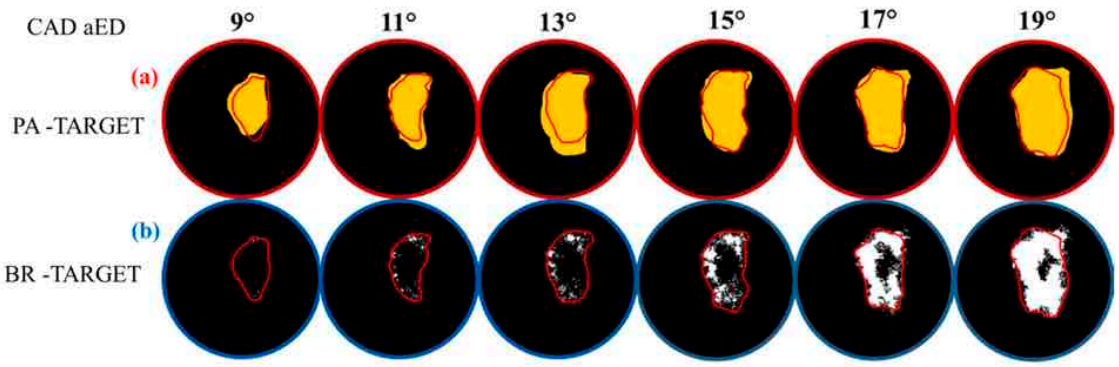

Figure 13. Comparison between (**a**) PA and (**b**) BR methods in determining the flame front in the first instants after the end of the discharge at $\lambda = 1.6$. The red lines on the images indicate the contour of the Target flame front whereas the yellow and white areas the flame front computed by PA and BR, respectively.

To this end, for each of the three engine operating conditions tested (Table 4), the corresponding confusion matrices were compiled. At each λ, Figures 14–16 report the comparisons between the flame front binarized areas of BR and the ones obtained by the compared algorithms. The overlap of the flame fronts is represented by white color, the flame overestimates with green one, whereas violet represents the underestimates made by the methods. The results obtained with PA achieve, on average, higher values of the three parameters. In particular, the PA Sensitivity is higher at each case analyzed, especially in darkest frames, i.e., during the kernel formation. Going into more detail, in the λ = 1.4 case, both methods have Specificity greater than 99%. This result testifies that the two algorithms are able to correctly identify those pixels not belonging to the edge, namely, not overestimations of the flame front are performed. However, the proposed method presents higher Sensibility levels, i.e., less flame front underestimations, especially after the end of discharge. This confirms the PA ability to better identify, from the beginning, the flame evolution if compared to the BR. The higher Accuracy (over 96%) of PA proves the greater capacity to correctly detect both pixels belonging and not belonging to the flame front. The above-mentioned differences between the compared methods are further emphasized at lean conditions. PA performed confusion matrix parameters extremely higher than BR, whose Sensitivity, in particular, is low in the first instants of flame evolution. For instance, at λ = 1.6, the first two images show Sensitivity levels less than 20%, as opposed to PA which instead shows values higher than 90%.

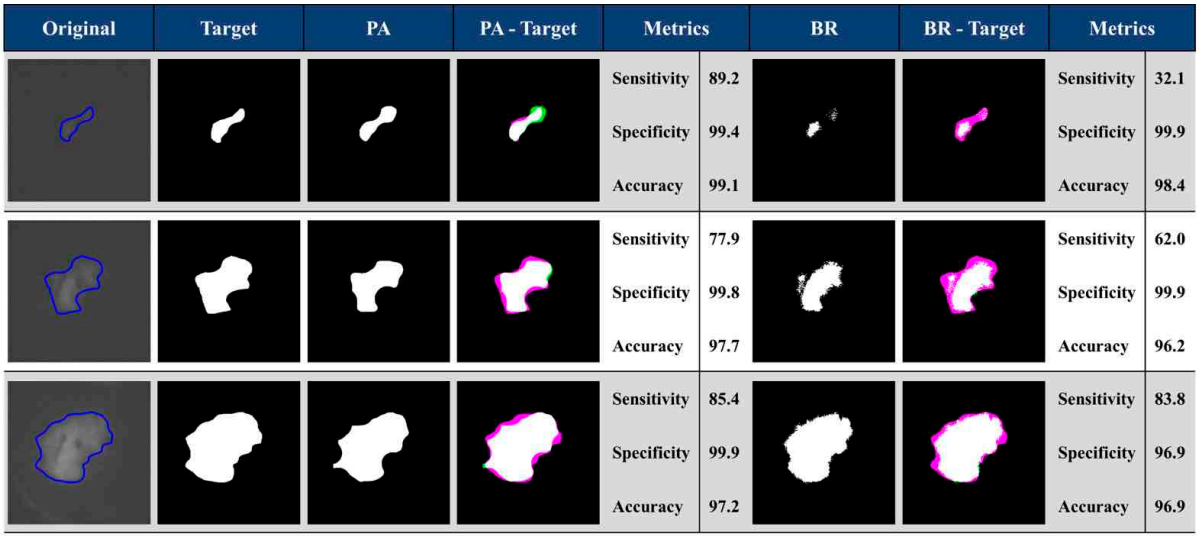

Figure 14. Evaluation of the metric at λ = 1.4 BDI.

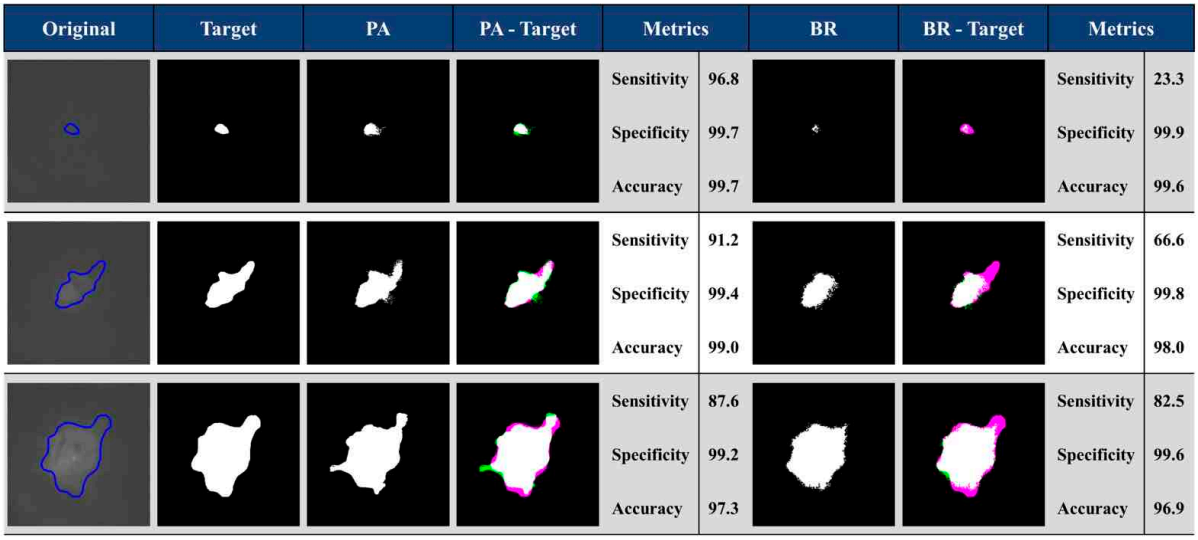

Figure 15. Evaluation of the metric at λ = 1.55 BDI.

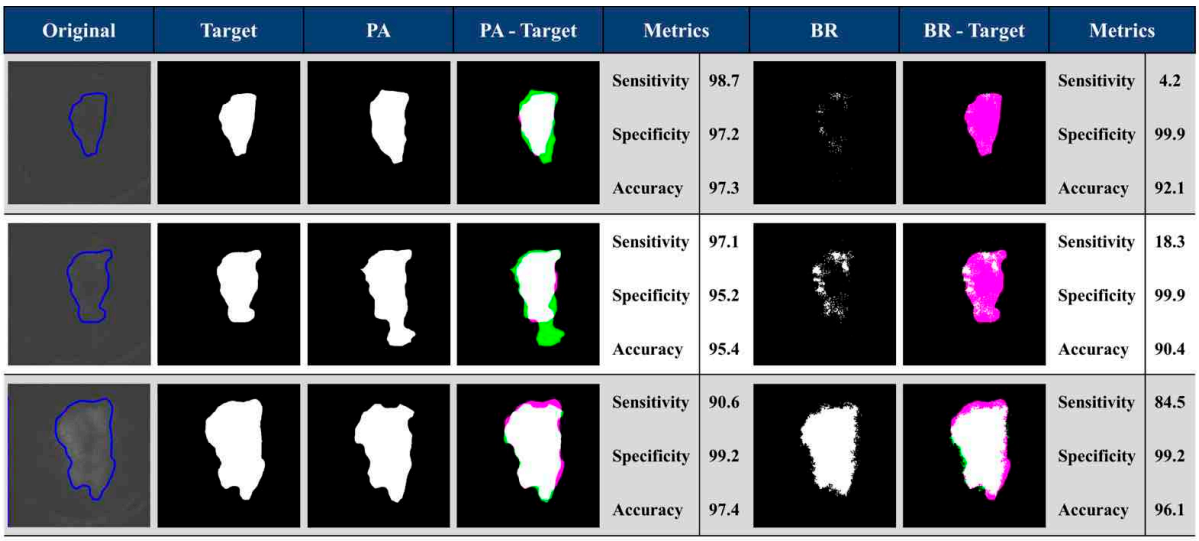

Figure 16. Evaluation of the metric at λ = 1.6 CSI.

6. Conclusions

This paper intends to propose a non-conventional method, based on the application of photographic techniques and a convolutional neural network, for the analysis of combustion events characterized by low-light conditions. The main target of this work is to improve the quality of the flame-front detection, starting from the first moments in which the kernel is generated. The proposed method was developed on image set of combustion events promoted by advanced corona ignition systems. The experimental campaign was carried out in a spark-ignition optical access engine and showed the capability of the ACIS devices to extend the lean stable limit of the engine with respect to the traditional spark (λ = 1.4). As the air/fuel ratio raises, the decreasingly luminosity of the flame front required a careful choice of the setting parameters of the previously utilized semiautomatic method and here used as a reference. This setting is needed to establish the correct threshold for the flame front area estimation, to perform the corresponding binarized area and, finally, to investigate the flame front evolution. Upon optimizing on a faint lean case, the PA algorithm was tested on the lean stable limits performed by the ACIS. The estimation of the equivalent frame radius R_{eq} was used to compare the results of both methods, with the ones related to images manually binarized by the user and used as a target.

1. Both algorithms were able to detect the flame front evolution by well reproducing the physical trend of the phenomenon. However, the PA curves bundles result in being less wide and therefore characterized by lower dispersion. Moreover, some combustions previously considered by the BR method as misfires or anomalies (3% of the total) are instead considered as physically valid by the proposed method. These features allow us to characterize the effective capability of the tested igniter on guarantying stable combustion onsets characterized by low cycle-to-cycle variability.
2. In all cases analyzed, both methods were able to correctly reproduce the Target trend, and, in particular, PA showed a greater capability to detect in advance (up to 1500 µs), the kernel formation if compared to BR. In this way, it is possible to carry out a more detailed analysis of the igniter's performance in the first moments of kernel formation. This feature is of pivotal importance at the leanest operating conditions of interest where BR showed its limits. Moreover, it allows for an almost-perfect correspondence between indicating and imaging analysis.
3. The metric parameters confirmed the capability of PA to allow more reliable detection of early flame kernel development. The proposed algorithm performed values of Accuracy, Sensitivity, and Specificity higher on average if compared to the BR one. The darker the case, the higher the differences with the BR method, which makes the PA method more suitable for analyzing ultra-lean combustions, towards which automotive research is increasingly focused.
4. Moreover, the capability of the PA algorithm to automatically estimate the binarization threshold allows us to perform an analysis of the flame front evolution completely independent from the user interpretation.

Author Contributions: Conceptualization, L.P. and F.R.; methodology, L.P. and F.R.; software, L.P. and F.R.; validation, L.P. and F.R.; formal analysis, L.P.; investigation, L.P. and F.R.; data curation, L.P. and F.R.; writing—original draft preparation, L.P. and F.R.; writing—review and editing, L.P., F.R., G.D. and F.M.; visualization, F.M.; supervision, F.M. and G.D.; project administration, F.M. All authors have read and agreed to the published version of the manuscript.

Funding: This research received no external funding.

Informed Consent Statement: Not applicable.

Conflicts of Interest: The authors declare no conflict of interest.

Nomenclature

ACIS	Advanced Corona Ignition System
IMEP	Indicated Mean Effective Pressure
aED	After End of Discharge
IT	Ignition Timing
AI	Artificial Intelligence
MBT	Maximum Brake Torque
BDI	Barrier Discharge Igniter
MFB	Mass Fraction Burned
BIMEF	Bio-Inspired Multi-Exposure Fusion
MFB50	50% of Mass Fraction Burned
BR	Base Reference method
ML	Machine Learning
CAD	Crank Angle Degree
OBD	On Board Diagnostic
CFD	Computational Fluid Dynamics
PFI	Port Fuel Injection
CNN	Convolutional Neural Network
PA	Proposed Algorithm
CoV_{IMEP}	Covariance of IMEP

R_{eq}	Equivalent flame radius
CSI	Corona Streamer-Type igniter
RF	Radio Frequency
DI	Direct Injection
SI	Spark Ignition
ECU	Engine Control Unit
TDC	Top Dead Center
EGR	Exhaust Gas Recirculation
t_{on}	Activation time of the igniter
FFDNet	Fast Flexible Denoising Network
TN	True Negative
FN	False Negative
TP	True Positive
FP	False Positive
V_d	Driving Voltage of the igniter
ICE	Internal Combustion Engine

Appendix A

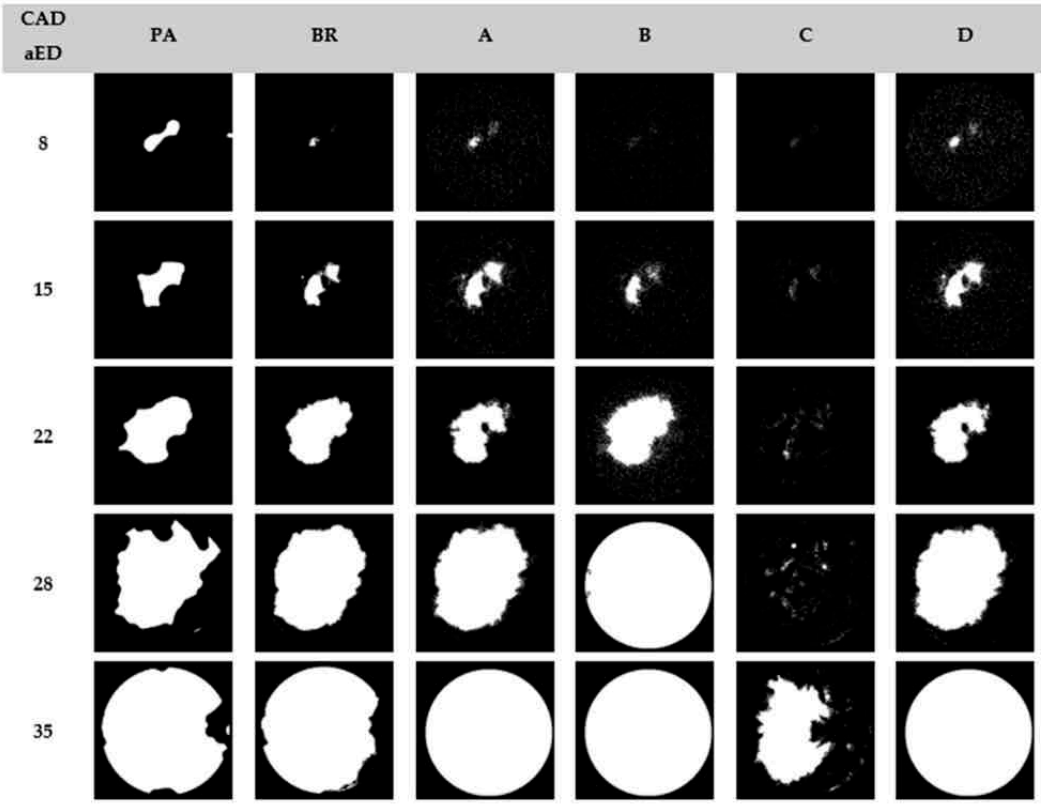

Figure A1. Binarized frames of BDI 1.4 air/fuel ratio for the different cases studied.

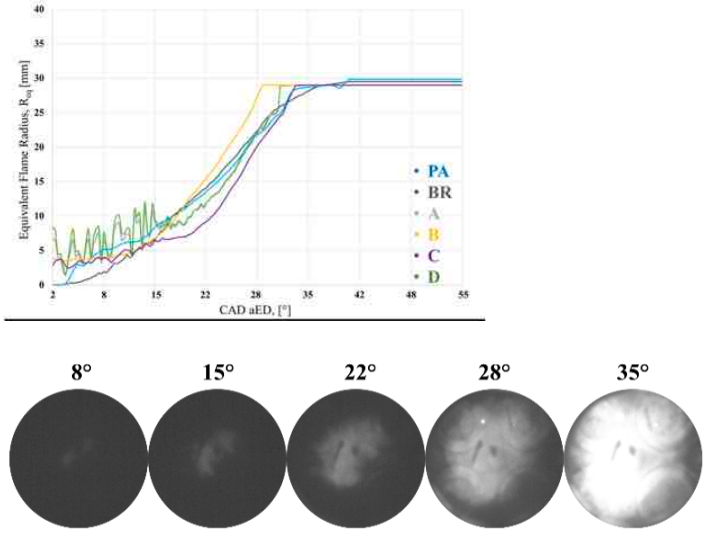

Figure A2. Equivalent radii for the cases studied in Table 2. Five images are showed in order to visual estimate the corresponding flame front propagation.

References

1. Gao, J.; Tian, G.; Sorniotti, A.; Karci, A.E.; di Palo, R. Review of thermal management of catalytic converters to decrease engine emissions during cold start and warm up. *Appl. Therm. Eng.* **2019**, *147*, 177–187. [CrossRef]
2. Alshammari, M.; Alshammari, F.; Pesyridis, A. Electric Boosting and Energy Recovery Systems for Engine Downsizing. *Energies* **2019**, *12*, 4636. [CrossRef]
3. Merola, S.S.; Marchitto, L.; Tornatore, C.; Valentino, G.; Irimescu, A. UV-visible Optical Characterization of the Early Combustion Stage in a DISI Engine Fuelled with Butanol-Gasoline Blend. *SAE Int. J. Engines* **2013**, *6*, 2638. [CrossRef]
4. Jeon, J.; Bock, N.; Northrop, W.F. In-cylinder Flame Luminosity Measured from a Stratified Lean Gasoline Direct Injection Engine. *Results Eng.* **2019**, *1*, 100005. [CrossRef]
5. Sher, E.; Ben-Ya'ish, J.; Pokryvailo, A.; Spector, Y. A Corona Spark Plug System for Spark-Ignition Engines. *SAE Tech. Pap.* **1992**, 920810. [CrossRef]
6. Varma, A.; Thomas, S. Simulation, Design and Development of a High Frequency Corona Discharge Ignition System. *SAE Tech. Pap.* **2013**, 1–10. [CrossRef]
7. Burrows, J.; Mixell, K.; Reinicke, P.B.; Riess, M.; Sens, M. Corona ignition—Assessment of physical effects by pressure chamber, rapid compression machine, and single cylinder engine testing. In Proceedings of the 2nd International Conference on Ignition Systems for Gasoline Engines, Berlin, Germany, 24–25 November 2014.
8. Mariani, A.; Foucher, F. Radio frequency spark plug: An ignition system for modern internal combustion engines. *Appl. Energy* **2014**, *122*, 151–161. [CrossRef]
9. Starikovskii, A.Y.; Anikin, N.B.; Kosarev, I.N.; Mintoussov, E.I. Nanosecond Pulsed Discharges for Plasma Assisted Combustion and Aerodynamics. *J. Propuls. Power* **2008**, *24*, 1182–1197. [CrossRef]
10. Sevik, J.; Wallner, T.; Pamminger, M.; Scarcelli, R. Extending Lean and Exhaust Gas Recirculation-Dilute Operating Limits of a Modern Gasoline Direct-Injection Engine Using a Low-Energy Transient Plasma Ignition System. *J. Eng. Gas Turbines Power* **2016**, *138*, 112807. [CrossRef]
11. Ikeda, Y.; Padala, S.; Makita, M.; Nishiyama, A. Development of Innovative Microwave Plasma Ignition System with Compact Microwave Discharge Igniter. *SAE Tech. Pap.* **2015**, 7. [CrossRef]
12. Idicheria, C.A.; Najt, P.M. Potential of Advanced Corona Ignition System (ACIS) for future engine applications. In *International Conference on Ignition Systems for Gasoline Engines*; Springer International Publishing: Cham, Switzerland, 2017; pp. 315–331. [CrossRef]
13. Marko, F.; König, G.; Schöffler, T.; Bohne, S.; Dinkelacker, F. Comparative optical and thermodynamic investigations of high frequency corona- and spark-ignition on a CV natural gas research engine operated with charge dilution by exhaust gas re- circulation. In *International Conference on Ignition Systems for Gasoline Engines*; Springer International Publishing: Cham, Switzerland, 2017; pp. 293–314. [CrossRef]
14. Cruccolini, V.; Discepoli, G.; Ricci, F.; Petrucci, L.; Grimaldi, C.; Papi, S.; Dal Re, M. Comparative Analysis between a Barrier Discharge Igniter and a Streamer-Type Radio-Frequency Corona Igniter in an Optically Accessible Engine in Lean Operating Conditions. *SAE Tech. Pap.* **2020**, 12. [CrossRef]
15. Ricci, F.; Petrucci, L.; Cruccolini, V.; Discepoli, G.; Grimaldi, C.N.; Papi, S. Investigation of the Lean Stable Limit of a Barrier Discharge Igniter and of a Streamer-Type Corona Igniter at Different Engine Loads in a Single-Cylinder Research Engine. *Multidiscip. Digit. Publ. Inst. Proc.* **2020**, *58*, 11. [CrossRef]

16. Ricci, F.; Zembi, J.; Battistoni, M.; Grimaldi, C.; Discepoli, G. *Experimental and Numerical Investigations of the Early Flame Development Produced by a Corona Igniter*; SAE Technical Paper 2019; SAE International: Warrendale, PA, USA, 2019. [CrossRef]
17. Fiifi, R.; Yan, F.; Kamal, M.; Ali, A.; Hu, J. Engineering Science and Technology, an International Journal Artificial neural network applications in the calibration of spark-ignition engines: An overview. *Eng. Sci. Technol. Int. J.* **2016**, *19*, 1346–1359. [CrossRef]
18. Çay, Y.; Çiçek, A.; Kara, F.; Sağiroğlu, S. Prediction of engine performance for an alternative fuel using artificial neural network. *Appl. Therm. Eng.* **2012**, *37*, 217–225. [CrossRef]
19. Atkinson, C.M. Virtual Sensing: A Neural Network-based Intelligent Performance and Emissions Prediction System for On-Board Diagnostics and Engine Control. *Prog. Technol.* **1998**, *73*, 2–4.
20. Pai, P.S.; Rao, B.R.S. Artificial Neural Network based prediction of performance and emission characteristics of a variable compression ratio CI engine using WCO as a biodiesel at different injection timings. *Appl. Energy* **2011**, *88*, 2344–2354. [CrossRef]
21. Arsie, I.; Cricchio, A.; de Cesare, M.; Lazzarini, F.; Pianese, C.; Sorrentino, M. Neural network models for virtual sensing of NOx emissions in automotive diesel engines with least square-based adaptation. *Control. Eng. Pract.* **2017**, *61*, 11–20. [CrossRef]
22. Rahimi Molkdaragh, R.; Jafarmadar, S.; Khalilaria, S.; Soukht Saraee, H. Prediction of the performance and exhaust emissions of a compression ignition engine using a wavelet neural network with a stochastic gradient algorithm. *Energy* **2018**, *142*, 1128–1138. [CrossRef]
23. Warey, A.; Gao, J. Prediction of Engine-Out Emissions Using Deep Convolutional Neural Networks. *SAE Tech. Pap.* **2021**, *3*, 2863–2871.
24. Salman, H.; Grover, J.; Shankar, T. Hierarchical Reinforcement Learning for Sequencing Behaviors. *Neural Comput.* **2018**, *2733*, 2709–2733. [CrossRef]
25. Simonyan, K.; Vedaldi, A.; Zisserman, A. Deep inside convolutional networks: Visualising image classification models and saliency maps. In Proceedings of the 2nd International Conference on Learning Representations, ICLR 2014—Workshop Track Proceedings, Banff, AB, Canada, 14–16 April 2014; pp. 1–8.
26. Soria, X.; Riba, E.; Sappa, A. Dense extreme inception network: Towards a robust CNN model for edge detection. In Proceedings of the 2020 IEEE Winter Conference on Applications of Computer Vision, WACV, Snowmass Village, CO, USA, 1–5 March 2020; pp. 1912–1921. [CrossRef]
27. He, J.; Zhang, S.; Yang, M.; Shan, Y.; Huang, T. Bi-directional cascade network for perceptual edge detection. In Proceedings of the IEEE Computer Society Conference on Computer Vision and Pattern Recognition, Long Beach, CA, USA, 15–20 June 2019; pp. 3823–3832. [CrossRef]
28. Gai, S.; Bao, Z. New image denoising algorithm via improved deep convolutional neural network with perceptive loss. *Expert Syst. Appl.* **2019**, *138*, 112815. [CrossRef]
29. Shahdoosti, H.R.; Rahemi, Z. Edge-preserving image denoising using a deep convolutional neural network. *Signal Processing* **2019**, *159*, 20–32. [CrossRef]
30. Shawal, S.; Goschutz, M.; Schild, M.; Kaiser, S.; Neurohr, M.; Pfeil, J.; Koch, T. High-speed imaging of early flame growth in spark-ignited engines using different imaging systems via endoscopic and full optical access. *SAE Int. J. Engines* **2016**, *9*, 704–718. [CrossRef]
31. Bhatti, S.S.; Verma, S.; Tyagi, S.K. Energy and Exergy Based Performance Evaluation of Variable Compression Ratio Spark Ignition Engine Based on Experimental Work. *Therm. Sci. Eng. Prog.* **2019**, *9*, 332–339. [CrossRef]
32. Irimescu, A.; Tornatore, C.; Marchitto, L.; Merola, S.S. Compression Ratio and Blow-by Rates Estimation Based on Motored Pressure Trace Analysis for an Optical Spark Ignition Engine. *Appl. Therm. Eng.* **2013**, *61*, 101–109. [CrossRef]
33. *SAE J1832_200102*; Low Pressure Gasoline Fuel Injector, SAE International Standard. SAE International: Warrendale, PA, USA, 2001. [CrossRef]
34. Ricci, F.; Cruccolini, V.; Discepoli, G.; Petrucci, L.; Grimaldi, C.; Papi, S. Luminosity and thermal energy measurement and comparison of a dielectric barrier discharge in an optical pressure-based calorimeter at engine relevant conditions. *SAE Tech. Pap.* **2021**, 11.
35. Romani, L.; Bianchini, A.; Vichi, G.; Bellissima, A.; Ferrara, G. Experimental Assessment of a Methodology for the Indirect in-Cylinder Pressure Evaluation in Four-Stroke Internal Combustion Engines. *Energies* **2018**, *11*, 1982. [CrossRef]
36. Cruccolini, V.; Discepoli, G.; Cimarello, A.; Battistoni, M.; Mariani, F.; Grimaldi, C.N.; Dal Re, M. Lean combustion analysis using a corona discharge igniter in an optical engine fueled with methane and a hydrogen-methane blend. *Fuel* **2020**, *259*, 116290. [CrossRef]
37. Cimarello, A.; Grimaldi, C.N.; Mariani, F.; Battistoni, M.; Dal Re, M. Analysis of RF Corona Ignition in Lean Operating Conditions Using an Optical Access Engine. *SAE Tech. Pap.* **2017**. [CrossRef]
38. Idicheria, C.A.; Yun, H.; Najt, P.M. An Advanced Ignition System for High Efficiency Engines. In Proceedings of the Ignition Systems for Gasoline Engines: 4th International Conference, Berlin, Germany, 6–7 December 2018; pp. 40–54. [CrossRef]
39. Pineda, D.I.; Wolk, B.; Chen, J.-Y.; Dibble, R.W. Application of Corona Discharge Ignition in a Boosted Direct-Injection Single Cylinder Gasoline Engine: Effects on Combustion Phasing, Fuel Consumption, and Emissions. *SAE Int. J. Engines* **2016**, *9*, 1970–1988. [CrossRef]
40. Discepoli, G.; Cruccolini, V.; Ricci, F.; di Giuseppe, A.; Papi, S.; Grimaldi, C.N. Experimental characterisation of the thermal energy released by a Radio-Frequency Corona Igniter in nitrogen and air. *Appl. Energy* **2020**, *263*, 114617. [CrossRef]

41. Cruccolini, V.; Grimaldi, C.N.; Discepoli, G.; Ricci, F.; Petrucci, L.; Papi, S. An Optical Method to Characterize Streamer Variability and Streamer-to-Flame Transition for Radio-Frequency Corona Discharges. *Appl. Sci.* **2020**, *10*, 2275. [CrossRef]
42. Ying, Z.; Li, G.; Gao, W. A bio-inspired multi-exposure fusion framework for low-light image enhancement. *arXiv* **2017**, arXiv:1711.00591.
43. Guo, X. LIME: A method for low-light image enhancement. In Proceedings of the 2016 ACM Multimedia Conference, Amsterdam, The Netherlands, 15–19 October 2016; pp. 87–91. [CrossRef]
44. He, X.; Cai, D.; Yan, S.; Zhang, H.-J. Neighborhood Preserving Embedding. In Proceedings of the Tenth IEEE International Conference on Computer Vision (ICCV'05) Volume 1, Beijing, China, 17–21 October 2005; Volume 2, pp. 1208–1213. [CrossRef]
45. Li, B.; Peng, X.; Wang, Z.; Xu, J.; Feng, D. (AOD-Net)—AOD-Net:All-in-one dehazing network boyi. In Proceedings of the IEEE International Conference on Computer Vision (ICCV), Venice, Italy, 22–29 October 2017; pp. 4770–4778.
46. Wang, Z.; Bovik, A.C.; Sheikh, H.R.; Simoncelli, E.P. Image quality assessment: From error visibility to structural similarity. *IEEE Trans. Image Processing* **2004**, *13*, 600–612. [CrossRef] [PubMed]
47. Horé, A.; Ziou, D. Image quality metrics: PSNR vs. SSIM. In Proceedings of the International Conference on Pattern Recognition, Istanbul, Turkey, 23–26 August 2010; pp. 2366–2369. [CrossRef]
48. Zhang, K.; Zuo, W.; Zhang, L. FFDNet: Toward a fast and flexible solution for CNN-Based image denoising. *IEEE Trans. Image Processing* **2018**, *27*, 4608–4622. [CrossRef]
49. Islam, M.Z.; Islam, M.M.; Asraf, A. A combined deep CNN-LSTM network for the detection of novel coronavirus (COVID-19) using X-ray images. *Inform. Med. Unlocked* **2020**, *20*, 100412. [CrossRef]